

Optical grade bromide-based thin film electrolytes

Nicola Melchioni^{1,2,*}, Giacomo Trupiano^{1,2}, Giorgio Tofani^{2,3}, Riccardo Bertini², Andrea Mezzetta³, Federica Bianco¹, Lorenzo Guazzelli³, Fabio Beltram¹, Christian Silvio Pomelli³, Stefano Roddaro², Alessandro Tredicucci^{1,2}, and Federico Paolucci^{1,4,†}

¹*NEST Laboratory, Istituto Nanoscienze CNR and Scuola Normale Superiore, Piazza San Silvestro 12, I-56127, Pisa, Italy*

²*Dipartimento di Fisica "E. Fermi", Università di Pisa, Largo Bruno Pontecorvo 3, I-56127, Pisa, Italy*

³*Dipartimento di Farmacia, Università di Pisa, Via Bonanno 33, 56126, Pisa, Italy*

⁴*INFN Sezione di Pisa, Largo Bruno Pontecorvo 3, I-56127 Pisa, Italy*

**Author to whom the correspondence should be addressed: nicola.melchioni@sns.it*

†*Electronic mail: federico.paolucci@pi.infn.it*

April 14, 2023

Abstract

Controlling the charge density in low-dimensional materials with an electrostatic potential is a powerful tool to explore and influence their electronic and optical properties. Conventional solid gates impose strict geometrical constraints to the devices and often absorb electromagnetic radiation in the infrared (IR) region. A powerful alternative is ionic liquid (IL) gating. This technique only needs a metallic electrode in contact with the IL and the highest achievable electric field is limited by the electrochemical interactions of the IL with the environment. Despite the excellent gating properties, a large number of ILs is hardly exploitable for optical experiments in the mid-IR region, because they typically suffer from low optical transparency and degradation in ambient conditions. Here, we report the realization of two electrolytes based on bromide ILs dissolved in polymethyl methacrylate (PMMA). We demonstrate that such electrolytes can induce state-of-the-art charge densities as high as $20 \times 10^{15} \text{ cm}^{-2}$. Thanks to the low water absorption of PMMA, they work both in vacuum and in ambient atmosphere after a simple vacuum

curing. Furthermore, our electrolytes can be spin coated into flat thin films with optical transparency in the range from 600 cm^{-1} to 4000 cm^{-1} . Thanks to these properties, the electrolytes are excellent candidates to fill the gap as versatile gating layers for electronic and mid-IR optoelectronic devices.

The possibility of controlling the charge density in an electron gas with electrostatic potentials (field-effect) unlocked many technologies at the basis of modern life. Such field-effect found new importance in experiments involving low-dimensional systems, such as 2D materials, Van der Waals heterostructures and nanowires. In those materials, a modification of the electronic density can have great impact on charge transport and infrared (IR) optical response [1, 2]. Moreover, field-effect dramatically influences the band structure of 2D crystals [3–8], since their few-atomic thickness prevents an efficient screening of the electric field created by the gate electrode. Conventionally, different solid-gate geometries are exploited, such as highly doped substrates covered with a dielectric (back-gate [9]), a dielectric deposited on the crystal hosting an electrode on top (top-gate [4]), lateral metallic pads on the same insulating substrate (side-gate [10]) or even Van der Waals heterostructures, where different layers act as gate electrode, dielectric and channel medium [11]. When dealing with optical experiments involving 2D materials and bulk semiconductors, such geometries are a limitation. Indeed, the high dielectric losses hinder the back-gating efficiency of the substrate, a top-gate would prevent adequate optical transparency, while side-gates do not grant the necessary spatial uniformity in the achievable charge density.

In this framework, ionic liquids (ILs) could be a versatile tool to overcome these restrictions. Indeed, ILs work independently from the surrounding environment and need only to be electrically contacted, thus being employable on fully insulating substrates and several gating geometries [12–15]. In the presence of a voltage between the channel and the gate electrode, the ions inside the IL arrange as charged layers at their surfaces. The electrostatic potential created by these ionic layers is screened by the attraction of charge carriers (electrons or holes) inside the channel and the gate electrode, thus forming the so-called electric double layers (EDLs) [16]. These EDLs are parallel plate capacitors with inter-plate distance of a few nm, thus offering an enhanced gating efficiency due to their high capacitance [17–19]. The generated electric fields up to 10 GV/m [20] allowed to explore unprecedented regimes, where deep modifications to the electronic properties were induced [21–24]. Moreover, while the dielectric breakdown restricts the efficiency of solid-state gates [25, 26], the main limitation of electrolyte gating is the electrochemical interaction of the IL with the surrounding environment [27]. For example, despite their high ionic transport efficiency, lithium-based electrolytes are expensive, highly reactive with most of other chemical substances [28] and scarcely compatible with polymer matrices. Differently, bromide-based ILs are widely available at accessible costs, polymer compatible, and at the same time thermally and electrochemically stable [29, 30]. However, most commercially available compounds are unstable under high voltage bias and exhibit poor transparency in the IR region [31–33].

In this Letter, we present the development of two new IR-transparent polymer electrolytes based on

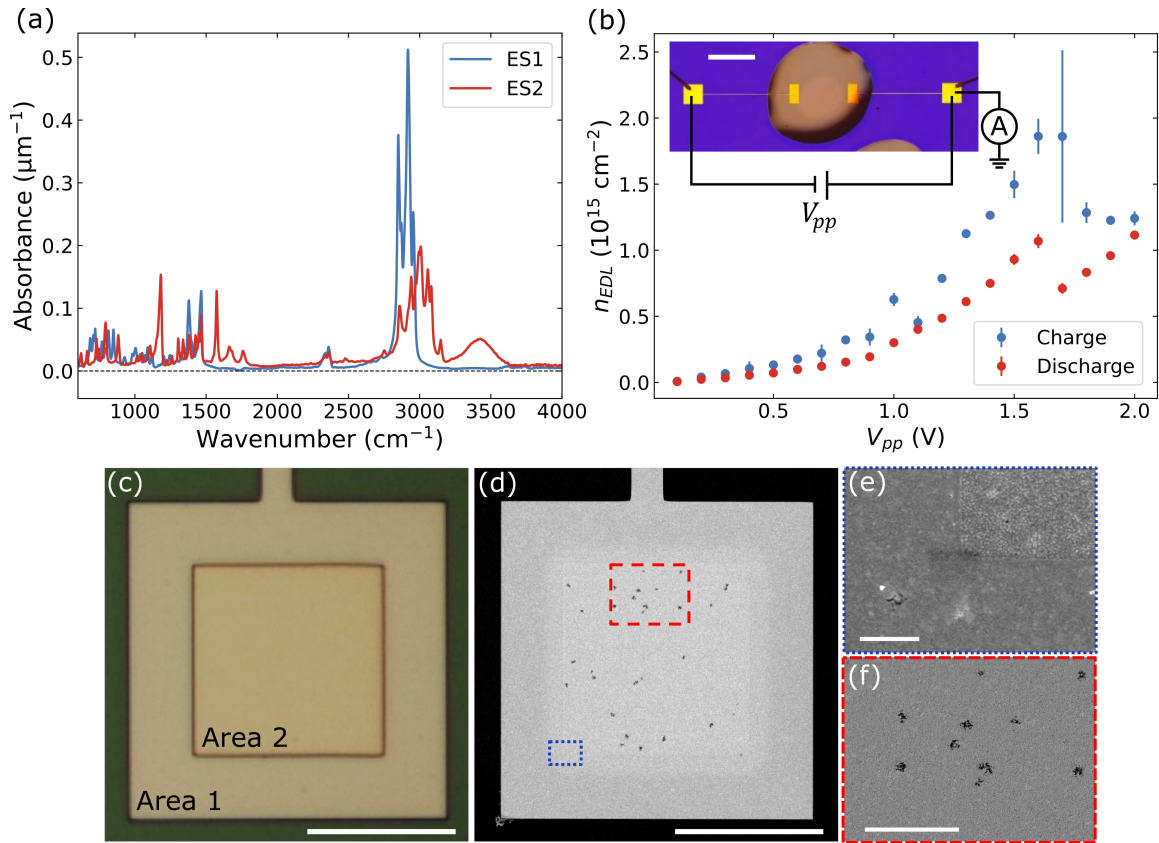


Figure 1: (a) Absorbance spectra of ES1 (blue solid line) and ES2 (red dashed line). (b) Charging (n_{EDL}^{ch} , blue dots) and discharging (n_{EDL}^{dch} , red dots) carrier density accumulated in the EDL in a drop of ES1 versus V_{pp} . Inset: optical image of the IL droplet on the metal pads employed for the transport measurements along with the experimental setup. The scalebar is $500 \mu\text{m}$. (c) Optical image of a pristine Cr/Au electrode. Area 1 is covered with a PMMA film, Area 2 is exposed to air and will be in direct contact with ES1. The scalebar is $100 \mu\text{m}$. (d) SEM image of the same electrode after the cycles of measurement in ambient conditions. The scalebar is $100 \mu\text{m}$. (e) Detail of a region between Area 1 and Area 2 (blue dotted square in (d)). The scalebar is $1 \mu\text{m}$. (f) Detail of Area 2 (red dashed square in (d)). The scalebar is $5 \mu\text{m}$.

bromide ionic liquids (br-ILs) dissolved in polymethyl methacrylate (PMMA). To this scope, we study their optical and charge transport properties when they are spin coated onto a substrate to form a thin film. In particular, we show that our electrolytes have large windows with $< 0.007 \mu\text{m}^{-1}$ absorption in the range from 600 cm^{-1} to 4000 cm^{-1} in air and are able to induced charge densities up to $\sim 20 \times 10^{15} \text{ cm}^{-2}$ in vacuum. Since their fabrication does not impose any geometrical restriction, our electrolytes can be employed as versatile transparent gates for low-dimensional materials in optical and optoelectronic experiments in the IR region. In addition, thanks to the flat surface, such electrolytic films might be an easily-accessible key element for a wide variety of experiments, such as light-matter interaction studies on mixed 2D-bulk semiconductor structures or double-gated systems at extreme charge concentrations. We first focus on the IR optical response and transport properties of two pure bromide-based ionic liquids

(ES1 and ES2). ES1 is commercial tetraoctylphosphonium bromide $[P(C8)_4Br]$ of purity $> 95\%$, while ES2 is 3,3'-(hexane-1,5-diyl)bis(1-methyl-1H-imidazolium)bromide $[C_6(MIM)_2/2Br]$. ES2 was synthesized using the standard ionic liquid synthesis procedure [34] adapted for dicationic ionic liquids [29]. A solution (2.1 equiv : 5 mL) of 1-methylimidazole (98%) in acetonitrile ($\geq 99\%$) was added dropwise under magnetic stirring to a solution (2 g, 1 equiv) of 1,6-dibromohexane (98%) in 10 mL of acetonitrile. The solution was stirred for 2 min and then the mixture was heated up and stirred at $80\text{ }^\circ\text{C}$ for 48 h. A white solid precipitation was observed after half an hour. The solvent was removed under reduced pressure and the obtained solid was washed 3 times with 10 mL of diethyl ether (99%+) and dried *in vacuo* at $65\text{ }^\circ\text{C}$.

To determine the IR optical properties of ES1 and ES2, two solid samples of the ILs were measured in a FTIR spectroscope with the Attenuated Total Reflection (ATR) method [35]. The measured absorbance spectrum of ES1 (blue solid line in Fig. 1a) shows an absorbance generally lower than $0.1\text{ }\mu\text{m}^{-1}$ in the range from 600 cm^{-1} to 2500 cm^{-1} , except for one sharp feature of $\sim 0.12\text{ }\mu\text{m}^{-1}$ at 1490 cm^{-1} . Higher absorbance peaks close to $0.5\text{ }\mu\text{m}^{-1}$ are visible below 3000 cm^{-1} . These peaks are attributed to the stretching vibrations of the $C_{sp3} - H_{x=1,2,3}$ groups present in tetraoctylphosphonium bromide [36]. Conversely, the absorbance spectrum of ES2 (red dashed line in Fig. 1a) shows more structured peaks up to $0.16\text{ }\mu\text{m}^{-1}$ in the region from 600 cm^{-1} to 2500 cm^{-1} and peaks around 3000 cm^{-1} lower with respect to ES1. These differences stem from the different cationic moiety of ES2, thus from the vibration modes of the imidazolium ring and from the stretching vibration of the shorter aliphatic chain and of the $C_{sp2} - H$, respectively [37]. In both spectra, the peaks around 2350 cm^{-1} are due to the absorption of CO_2 in the atmosphere and are not related to the ILs.

We now focus on the ionic transport properties of ES1. To this scope, we fabricated metallic electrodes on top of boron-doped Si substrates covered with 300 nm of thermally grown SiO_2 by electron beam lithography (EBL) and thermal evaporation of 7 nm of chromium and 50 nm of gold (see the inset of Fig. 1b). The transport properties of pure ES1 were investigated by Double Step Chronocoulometry [38] (DSC, see Fig. S2 in SI) in ambient conditions. Thus, the accumulated charge in the EDL (Q_{EDL}) were determined both during its charging (*ch*) and discharging (*dch*). Then, the values of Q_{EDL} were divided by the electrode area and by the electronic charge to extract the charge carrier density accumulated in (removed from) the EDL, i.e. n_{EDL}^{ch} (n_{EDL}^{dch}). Figure 1b reports n_{EDL}^{ch} and n_{EDL}^{dch} as a function of the applied potential (V_{pp}) for ES1. The accumulated charge density grows with V_{pp} until reaching a value of $\sim 1.8 \times 10^{15}\text{ cm}^{-2}$ for $V_{pp} = 1.6\text{ V}$. For larger V_{pp} , the accumulated charge decreases. Such behaviour is the result of the electrochemical activity of the system. Indeed, the upper limit of the electrochemical window [39] of

ES1 is ~ 1.25 V (see Fig S3 in SI). When the applied voltage exceeds such value, reduction/oxidation reactions start to take place at the interface between the liquid and the electrodes [27, 40], effectively reducing the charge accumulated in the EDL. Moreover, water from the atmosphere can dissolve in ES1. When applying a voltage bias, the absorbed water reacts with the bromide in the IL forming an acid environment [41]. Consequently, part of the Br^- anions involved in these reactions do not participate to the charging of the EDL. The electrochemical activity of the liquid generates a difference between the charging and the discharging of the EDL (red dots in Fig. 1b). In particular, $Q_{EDL}^{ch} \sim 1.7Q_{EDL}^{dch}$ for all values of $V_{pp} < 1.6$ V (see Fig. S4 in SI). This asymmetry can be partially linked to the mobility of the ions in the IL, since the ionic mobility depends on the driving field and it changes when a voltage is applied with respect to the zero-bias condition [42]. However, the largest difference is observed for $V_{pp} = 1.7$ V, just above the electrochemical window limit, and the difference lowers as the voltage is increased. This behaviour suggests that the change in the ionic mobility, which should be increased by the higher applied voltage, has in fact minor effects with respect to the reactions.

To better understand the interaction between the liquid and the electrodes, the experiment was repeated on a device with electrodes partially covered by a PMMA with opening fabricated by EBL (see Fig. 1c). After the transport measurements, ES1 and the PMMA mask were removed with acetone and the electrodes observed under a scanning electron microscope (SEM). The contrast between the two regions shows that the morphology of the metallic film that was in contact with ES1 is dramatically different from the one of the masked metal (see Fig. 1d), thus confirming that the ionic liquid chemically interacted with the electrodes. In addition, a $10\text{-}\mu\text{m}$ -wide transitional region is visible, due to the IL diffusion below the PMMA mask (see Fig. 1e). In the region exposed to ES1, the overall roughness is increased and holes are present in the metallic film (see Fig. 1f). Such observation suggests that the electrochemically formed bromide-based acids attack the electrodes when applying a voltage. Indeed, the interaction of bromide with water absorbed from the atmosphere can create hypobromous acid (HOBr) and hydrobromic acid (HBr) [43]. Both acids attack gold [44], thus degrading the electrodes and reducing the gating effectiveness of the liquid. As a consequence, when voltages are applied to the liquid in ambient atmosphere, electrochemical reactions happen also within the electrochemical window. However, when water is removed from the liquid, the electrochemical window widens and such reactions are avoided (see Fig. S3 in SI).

Since PMMA can absorb only a small amount of water ($\sim 2\%$ w/w)[45], we exploit it to embed the bromide-based ILs and prevent the creation of an acid environment destructive for the devices. Furthermore, a spin-coated electrolyte thin film improves the device optical properties thanks to its lower thickness and higher flatness. Therefore, we investigated both the optical and charge transport properties

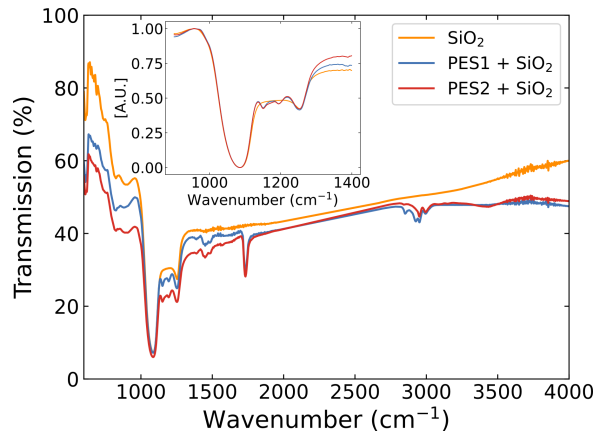


Figure 2: Transmission spectrum of a Si/SiO₂ chip (orange line) compared to the transmission of the same substrate with PES1 (blue line) and PES2 (red line) on top. Inset: zoom of the signals in the region around the SiO₂ phonons. The minima were shifted to 0 and the signals normalized on their maxima for a better comparison of the shape.

of the ILs when embedded in the PMMA matrix. To this scope we synthesised two polymer electrolytes (PES1 and PES2) starting from ES1 and ES2. PES1 is produced by dissolving 4.30 mg of ES1 in 430 mg of AR 679.04 950K (ethyl lactate solution of PMMA 950K at 4%, AllResist), while PES2 is realized by dissolving 6.10 mg of ES2 in 612 mg of AR 679.04 950K. Both solutions are therefore 25% mg IL/mg PMMA.

To demonstrate the suitability of PESs in optical experiments, we measured the optical transmission of a structure composed by a PES film spin coated onto Si/SiO₂ substrates (4000 rpm for 1 minute, soft baked at 100 °C for 2 minutes, thickness \sim 290 nm, see Fig. S1 in SI). In general, the PES/SiO₂/Si transmission spectra show a reduction of the transmitted power of \sim 5 – 10% with respect to the bare substrate (see Fig. 2). This reduction is due to the absorption in the film and to reflection effects caused by the air/PES and PES/SiO₂ interfaces. The baseline is also influenced by thin film effects [46], visible as a downward bending in the higher region of the spectra. Transmission dips related to PESs are present in the region 1200-1800 cm⁻¹. These lines are mainly attributed to the deformation vibrations of the (O)CH₃ and ester groups in the PMMA film [47] and are very similar for both PES1 and PES2. Instead, the two spectra differ in the region close to 3000 cm⁻¹, where the resonances are originated by the strain vibration of CH_{x=1,2,3} groups [48]. Thus, the reduced transmission in the PESs film can be attributed to the different distribution of the CH_{x=1,2,3} groups in the films due to the presence of the ESs. Nevertheless, the general features of the transmission spectrum of the bare substrate are preserved, such as the characteristic SiO₂ phonons at 1084 cm⁻¹ and 1256 cm⁻¹ [49] see inset of Fig. 2).

Generally, the charge transport properties of the electrolytes are modified when they are embedded in a

polymer matrix [50–54] especially when they are in form of a thin film [55]. Indeed, the ionic transport is mediated by large molecules that migrate through the polymeric matrix. For example, amorphous polymers offer larger inter-molecular cavities for ions migration with respect to ordered polymers [56]. The dimension of inter-molecular cavities is also influenced by ion size [57] and by the employed solvent [58]. To test the suitability of our polymer electrolytes as gating materials, we performed DSC experiments on both PES1 and PES2. In the form of a thin film, PES1 showed a poor ionic transport, thus we focused on PES2. Figure 3a shows the charge density accumulated in the EDL formed by a PES2 film as a function of the applied voltage V_{pp} both in ambient and vacuum conditions. In ambient conditions, the accumulated charge density reaches up to $2 \times 10^{15} \text{ cm}^{-2}$ for positive voltages and $4 \times 10^{15} \text{ cm}^{-2}$ for negative voltages (blue dots in Fig. 3a). A nominally identical sample was investigated in vacuum at a pressure of $\sim 10^{-5}$ mbar (red dots in Fig. 3a). The accumulated charge density is much higher in vacuum than in air pressure: $n_{EDL}^{vac}/n_{EDL}^{air} \sim 19.7$ for $V_{pp} = 0.5 \text{ V}$ and ~ 8.6 for $V_{pp} = -0.5 \text{ V}$. The higher accumulated charge density in vacuum is attributed to the increased ion mobility as a consequence of two concurring factors. First, when PSEs are in vacuum, contaminant gaseous molecules such as water are expelled from the material. Second, the reduced pressure on the surface allows for the structure to relax, thus creating wider paths for ions to migrate. The asymmetry measured for positive and negative values of the applied potential in vacuum can be attributed to the difference of cations and anions dimension in the liquid. Similarly to pure ES1 (see Fig. 1b), the induced charge density grows following a monotonic trend until $|V_{pp}| \sim 0.9 \text{ V}$. After that threshold, the ions in the electrolyte start interacting with the polymer matrix and the electrodes, thus modifying the EDL charging efficiency.

Despite the IL being embedded in PMMA, an acid environment is created when applying a DC bias to PES2 in ambient conditions, as measured for bare ES1 (see Fig. 1c-f). This acid environment modifies the morphology of the device electrodes, as clearly observable in Fig. 3b. Conversely, when PES2 is measured in vacuum, the electrodes are preserved from electrochemical damaging (Fig. 3c). This indicates the small amount of water trapped by the PMMA film in ambient conditions is sufficient to create HOBr and/or HBr. Instead, in vacuum, the film expels most of the absorbed water, thus preventing the formation of the acid environment.

After removing the water by keeping the device in vacuum, we test the stability of the PES structure by performing consecutive DSC cycles with a fixed $V_{pp} = 300 \text{ mV}$ in ambient conditions. As shown in Fig. 4a, the accumulated charge density n_{EDL}^N is highly stable for the first 6 cycles. Here, n_{EDL}^N is the accumulated charge density at cycle N normalized by the carrier concentration accumulated during the first cycle. After these cycles, n_{EDL}^N increases of a factor ~ 1.3 . This increase can be tentatively explained

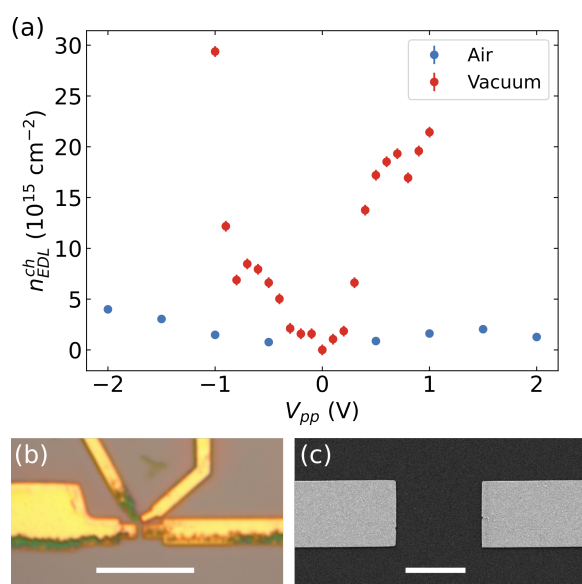


Figure 3: (a) Charge density accumulated in the EDLs in PES2 when in ambient conditions (blue) and vacuum (orange) versus V_{pp} . (b) Optical image of the metallic electrodes employed for the measurement in ambient conditions. The scalebar is 5 μm . (c) SEM image of the metallic electrodes employed for measurement in vacuum. The scalebar is 10 μm .

by considering that, when the polymer is brought back at air conditions, the reduction of polymer film volume caused by the air pressure leads to a decrease of the the paths for the ions migration. Consequently, during the first few cycles, the ions are pushed through the polymer matrix and open back accessible paths for the charge migration. As a result, the charge accumulated in the EDL increases after a few cycles, as similarly occurs for lithium intercalation in bilayer graphene [59, 60]. It is worth to notice that, differently from previous experiments, the applied potential does not damage the electrodes, as shown in Fig. 4b. Interestingly, the macroscopic morphology of the PES2 film changes after the application of voltages in ambient conditions after the vacuum treatment. Indeed, bias-induced cracks appear over the surface of the polymer, mainly starting from points where the film was already damaged, such as near the bonding wires or metallic residues, (see Fig. 4b and S5 in SI). Indeed, the water molecules can efficiently penetrate into the PMMA film from these points. Within these cracks, Br- based acids can be electrochemically created and gradually diffuse through the polymer matrix. In full agreement with the DSC measurements, Fig. 4b shows that even when the cracks are formed, the electrodes are not degraded, suggesting that negligible chemical interactions took place. Therefore, removing the water content from the polymer matrix before any voltage is applied enhances the robustness of polymer-embedded ionic liquids. Indeed, a simple treatment in vacuum preparation ensures a large stability of the accumulated charge density and prevents the formation of an acid environment in the proximity of the metallic electrodes even

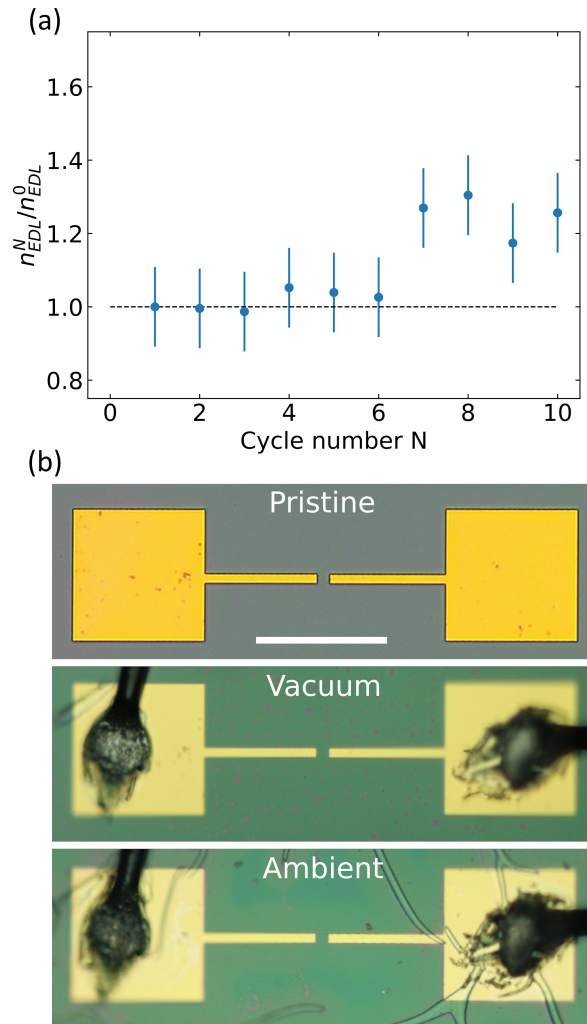


Figure 4: (a) Charge density accumulated in consecutive cycles performed on PES2 in ambient conditions at $V_{pp} = 300$ mV after the measurements in vacuum. (b) Optical images of the metallic pads used in the chronocoulometry measurements before PES2 is spun (top), after the measurement in vacuum (middle) and after the measurement in air (bottom). The scalebar is $150 \mu\text{m}$. The bonding wires used for electrical measurements are visible on the gold pads in the middle and bottom images.

when employed for several cycles in air. In summary, we proposed and demonstrated a new class of polymer-embedded bromide-based ionic liquids. The EDLs that form when the films are polarized can accumulate state-of-the-art charge densities up to $\sim 20 \times 10^{15} \text{ cm}^{-2}$ [15]. Furthermore, these electrolytes are transparent in the mid-infrared region of the spectrum and can be easily spin coated in the form of a thin film, thus providing remarkable advantages in optoelectronic devices. Although bromide based ILs react with water to form acids chemically attacking the electrodes, we demonstrated that it is possible to remove the absorbed water by a vacuum treatment before any voltage is applied, thus preventing the degradation of the metals. Furthermore, the polymer matrix of PMMA embedded ILs protects the electrodes for several cycles in ambient conditions after the vacuum curing. Therefore, devices exploiting

our electrolytes can be fabricated with standard techniques in ambient conditions without the need of the inert atmosphere of a glove box, as usually necessary for lithium based ILs [18, 19, 59, 60].

Acknowledgments

Fe.B. acknowledges the project q-LIMA in the framework of the PRIN2020 initiative of the Italian Ministry of University and Research for partial financial support. Gio.T., A.M., L.G., C.S.P. and S.R. acknowledge the project Quantum2D in the framework of the PRIN2017 initiative of the Italian Ministry of University and Research for partial financial support.

Data Availability

All the data are available upon request to the corresponding author.

Conflict of Interests

The authors have no conflicts to disclose.

References

- (1) Yan, H.; Xia, F.; Zhu, W.; Freitag, M.; Dimitrakopoulos, C.; Bol, A. A.; Tulevski, G.; Avouris, P. *ACS Nano* **2011**, *5*, 9854–9860.
- (2) Grigorenko, A.; Polini, M.; Novoselov, K. *Nature Photonics* **2012**, *6*, 749–758.
- (3) Oostinga, J. B.; Heersche, H. B.; Liu, X.; Morpurgo, A. F.; Vandersypen, L. M. K. *Nature Materials* **2008**, *7*, 151–157.
- (4) Zhang, Y.; Tang, T.-T.; Girit, C.; Hao, Z.; Martin, M. C.; Zettl, A.; Crommie, M. F.; Shen, R.; Wang, F. *Nature* **2009**, *459*, 820–823.
- (5) Dai, X.; Li, W.; Wang, T.; Wang, X.; Zhai, C. *Journal of Applied Physics* **2015**, *117*, 084310.
- (6) Kim, J.; Baik, S. S.; Ryu, S. H.; Sohn, Y.; Park, S.; Park, B.-G.; Denlinger, J.; Yi, Y.; Choi, H. J.; Kim, K. S. *Science* **2015**, *349*, 723–726.

- (7) Forsythe, C.; Zhou, X.; Watanabe, K.; Taniguchi, T.; Pasupathy, A.; Moon, P.; Koshin, M.; Kim, P.; Dean, C. R. *Nature Nanotechnology* **2018**, *13*, 566–571.
- (8) Chen, P. et al. *Applied Physics Letters* **2019**, *115*, 083104.
- (9) Lemme, M. C.; Echtermeyer, T. J.; Baus, M.; Kurz, H. *IEEE Electron Device Letters* **2007**, *28*, 282–284.
- (10) Robinson, L. A. W.; Lee, S.-B.; Teo, K. B. K.; Chhowalla, M.; Amaratunga, G. A. J.; Milne, W. I.; Williams, D. A.; Hasko, D. G.; Ahmed, H. *Nanotechnology* **2003**, *14*, 290.
- (11) Novoselov, K. S.; Mishchenko, A.; Carvalho, A.; Neto, A. H. C. *Science* **2016**, *353*, aac9439.
- (12) Lu, C.; Fu, Q.; Huang, S.; Liu, J. *Nano Letters* **2004**, *4*, 623–627.
- (13) Misra, R.; McCarthy, M.; Hebard, A. F. *Applied Physics Letters* **2007**, *90*, 052905.
- (14) Segawa, K.; Ren, Z.; Sasaki, S.; Tsuda, T.; Kuwabata, S.; Ando, Y. *Phys. Rev. B* **2012**, *86*, 075306.
- (15) Piatti, E. *Nano Express* **2021**, *2*, 024003.
- (16) Fujimoto, T.; Awaga, K. *Phys. Chem. Chem. Phys.* **2013**, *15*, 8983–9006.
- (17) Zhang, H.; Berthod, C.; Berger, H.; Giamarchi, T.; Morpurgo, A. F. *Nano Letters* **2019**, *19*, 8836–8845.
- (18) Gonnelli, R. S.; Piatti, E.; Sola, A.; Tortello, M.; Dolcini, F.; Galasso, S.; Nair, J. R.; Gerbaldi, C.; Cappelluti, E.; Bruna, M.; Ferrari, A. C. *2D Materials* **2017**, *4*, 035006.
- (19) Daghero, D.; Paolucci, F.; Sola, A.; Tortello, M.; Ummarino, G. A.; Agosto, M.; Gonnelli, R. S.; Nair, J. R.; Gerbaldi, C. *Physical Review Letters* **2012**, *108*, 066807.
- (20) Weintrub, B. I.; Hsieh, Y.-L.; Kovalchuk, S.; Kirchhof, J. N.; Greben, K.; Bolotin, K. I. *Nature Communications* **2022**, *13*, 6601.
- (21) Ye, J. T.; Zhang, Y. J.; Akashi, R.; Bahramy, M. S.; Arita, R.; Iwasa, Y. *Science* **2012**, *338*, 1193–1196.
- (22) Wang, S.; Ha, M.; Manno, M.; Frisbie, C. D.; Leighton, C. *Nature Communications* **2012**, *3*, DOI: 10.1038/ncomms2213.
- (23) Ponomarev, E.; Ubrig, N.; Gutiérrez-Lezama, I.; Berger, H.; Morpurgo, A. F. *Nano Letters* **2018**, *18*, 5146–5152.
- (24) Domaretskiy, D.; Philippi, M.; Gibertini, M.; Ubrig, N.; Gutiérrez-Lezama, I.; Morpurgo, A. F. *Nature Nanotechnology* **2022**, *17*, 1078–1083.

- (25) Murrell, M. P.; Welland, M. E.; O'Shea, S. J.; Wong, T. M. H.; Barnes, J. R.; McKinnon, A. W.; Heyns, M.; Verhaverbeke, S. *Applied Physics Letters* **1993**, *62*, 786–788.
- (26) Hattori, Y.; Taniguchi, T.; Watanabe, K.; Nagashio, K. *ACS Applied Materials & Interfaces* **2016**, *8*, 27877–27884.
- (27) Zhao, S.; Zhou, Z.; Peng, B.; Zhu, M.; Feng, M.; Yang, Q.; Yan, Y.; Ren, W.; Ye, Z.-G.; Liu, Y.; Liu, M. *Advanced Materials* **2017**, *29*, 1606478.
- (28) Sheng, L.; Wang, Q.; Liu, X.; Cui, H.; Wang, X.; Xu, Y.; Li, Z.; Wang, L.; Chen, Z.; Xu, G.; Wang, J.; Tang, Y.; Amine, K.; Xu, H.; He, X. *Nature Communication* **2022**, *13*, 172.
- (29) Ferdeghini, C.; Guazzelli, L.; Pomelli, C. S.; Ciccioli, A.; Brunetti, B.; Mezzetta, A.; Vecchio Cipriotti, S. *Journal of Molecular Liquids* **2021**, *332*, 115662.
- (30) Vraneš, M.; Papović, S.; Rackov, S.; Alenezi, K.; Gadžurić, S.; Tot, A.; Pilić, B. *The Journal of Chemical Thermodynamics* **2019**, *139*, 105871.
- (31) Piatti, E.; Guglielmero, L.; Tofani, G.; Mezzetta, A.; Guazzelli, L.; D'Andrea, F.; Roddaro, S.; Pomelli, C. S. *Journal of Molecular Liquids* **2022**, *364*, 120001.
- (32) Palumbo, O.; Cimini, A.; Trequattrini, F.; Brubach, J.-B.; Roy, P.; Paolone, A. *Phys. Chem. Chem. Phys.* **2020**, *22*, 7497–7506.
- (33) Moumene, T.; Belarbi, E. H.; Haddad, B.; Villemin, D.; Abbas, O.; Khelifa, B.; Bresson, S. *Journal of Molecular Structure* **2014**, *1065-1066*, 86–92.
- (34) Chiappe, C.; Mezzetta, A.; Pomelli, C. S.; Puccini, M.; Seggiani, M. *Organic Process Research & Development* **2016**, *20*, 2080–2084.
- (35) Mendoza-Galván, A.; Méndez-Lara, J. G.; Mauricio-Sánchez, R. A.; Järrendahl, K.; Arwin, H. *Opt. Lett.* **2021**, *46*, 872–875.
- (36) Silverstein, R. M.; Webster, F. X.; Kiemle, D. J.; Bryce, D. L., *Spectrometric Identification of Organic Compounds, 8th edition*; Wiley: 2014.
- (37) Yamada, T.; Tominari, Y.; Tanaka, S.; Mizuno, M. *The Journal of Physical Chemistry B* **2017**, *121*, 3121–3129.
- (38) Inzelt, G. In *Electroanalytical Methods: Guide to Experiments and Applications*, Scholz, F., Bond, A., Compton, R., Fiedler, D., Inzelt, G., Kahlert, H., Komorsky-Lovrić, Š., Lohse, H., Lovrić, M., Marken, F., Neudeck, A., Retter, U., Scholz, F., Stojek, Z., Eds.; Springer Berlin Heidelberg: Berlin, Heidelberg, 2010, pp 147–158.

- (39) Hayyan, M.; Mjalli, F. S.; Hashim, M. A.; AlNashef, I. M.; Mei, T. X. *Journal of Industrial and Engineering Chemistry* **2013**, *19*, 106–112.
- (40) Girault, H. H., *Analytical and Physical Electrochemistry*, 1st Edition; EPFL Press: 2004.
- (41) Shkrob, I. A.; Marin, T. W.; Crowell, R. A.; Wishart, J. F. *The Journal of Physical Chemistry A* **2013**, *117*, 5742–5756.
- (42) Clark, R.; von Domaros, M.; McIntosh, A. J. S.; Luzar, A.; Kirchner, B.; Welton, T. *The Journal of Chemical Physics* **2019**, *151*, 164503.
- (43) Sivey, J. D.; Arey, J. S.; Tentscher, P. R.; Roberts, A. L. *Environmental Science & Technology* **2013**, *47*, 1330–1338.
- (44) Walker, P.; Tarn, W. H., *CRC handbook of metal etchants*; CRC press: 1990.
- (45) N'Diaye, M.; Pascaretti-Grizon, F.; Massin, P.; Baslé, M. F.; Chappard, D. *Langmuir* **2012**, *28*, 11609–11614.
- (46) El-Menyawy, E.; El-Ghamaz, N.; Nawar, H. *Journal of Molecular Structure* **2013**, *1036*, 144–150.
- (47) Jitian, S.; Bratu, I. *AIP Conference Proceedings* **2012**, *1425*, 26–29.
- (48) Jeon, Y.; Sung, J.; Seo, C.; Lim, H.; Cheong, H.; Kang, M.; Moon, B.; Ouchi, Y.; Kim, D. *The Journal of Physical Chemistry B* **2008**, *112*, 4735–4740.
- (49) Lehmann, A.; Schumann, L.; Hübner, K. *Physica Status Solidi B* **1983**, *117*, 689–698.
- (50) Mogurampelly, S.; Ganesan, V. *The Journal of Chemical Physics* **2017**, *146*, 074902.
- (51) Ganesan, V. *Mol. Syst. Des. Eng.* **2019**, *4*, 280–293.
- (52) Vargas-Barbosa, N. M.; Roling, B. *ChemElectroChem* **2020**, *7*, 367–385.
- (53) Xiao, W.; Yang, Q.; Zhu, S. *Sci. Rep.* **2020**, *10*, DOI: 10.1038/s41598-020-64689-8.
- (54) Fong, K. D.; Self, J.; McCloskey, B. D.; Persson, K. A. *Macromolecules* **2021**, *54*, 2575–2591.
- (55) Zhao, Q.; Bennington, P.; Nealey, P. F.; Patel, S. N.; Evans, C. M. *Macromolecules* **2021**, *54*, 10520–10528.
- (56) Ramesh, S.; Liew, C.-W.; Ramesh, K. *Journal of Non-Crystalline Solids* **2011**, *357*, 2132–2138.
- (57) Shen, K.-H.; Hall, L. M. *Macromolecules* **2020**, *53*, 10086–10096.
- (58) Sharick, S.; Koski, J.; Riggelman, R. A.; Winey, K. I. *Macromolecules* **2016**, *49*, 2245–2256.
- (59) Kühne, M.; Paolucci, F.; Popovic, J.; Ostrovsky, P.; Maier, J.; Smet, J. *Nature Nanotechnology* **2017**, *12*, 895–900.

- (60) Zielinski, P.; Kühne, M.; Kärcher, D.; Paolucci, F.; Wochner, P.; Fecher, S.; Drnec, J.; Felici, R.; Smet, J. H. *Nano Letters* **2019**, *19*, 3634–3640.